Journal of Materials Research and Technology 36 (2025) 9168–9181

Contents lists available at ScienceDirect

Journal of Materials Research and Technology

journal homepage: www.elsevier.com/locate/jmrt

Sm_2O_3-induced superconductivity enhancements in bulk Y-123 ceramics synthesized via a novel modified thermal decomposition method

Ryad Alhadei Mohamed Arebat [a,b], Mohd Mustafa Awang Kechik [a,*], Yap Siew Hong [a], Chen Soo Kien [a], Lim Kean Pah [a], Hussien Baqiah [c], Fatma Barood [d], Syahrul Humaidi [e], Hoo Keong Peh [a], Abdul Halim Shaari [a], Muhammad Kashfi Shabdin [a], Muralidhar Miryala [f]

[a] Superconductor & Thin Films Laboratory, Department of Physics, Faculty of Science, Universiti Putra Malaysia, UPM Serdang, 43400, Selangor, Malaysia
[b] Department of Physics, Faculty of Science, El-Mergib University, Al Khums City, Libya
[c] Shandong Key Laboratory of Biophysics, Institute of Biophysics, Dezhou University, No. 566 University Rd. West, Dezhou, Shandong, China
[d] Department of Physics, Faculty of Science, Azzaytuna University, Tarhuna City, Libya
[e] Postgraduate Program (Physics), FMIPA, Universitas Sumatera Utara, Medan, 20222, Indonesia
[f] Materials for Energy and Environmental Laboratory, Superconducting Materials, Shibaura Institute of Technology, 3 Chome-7-5 Toyosu, Koto, Tokyo, 135-8548, Japan

ARTICLE INFO

Handling Editor: L Murr

Keywords:
Y-123 ceramics
Sm_2O_3 addition
Modified thermal decomposition (MTD)
Phase formation
Critical current density (J_c)
Superconductivity enhancement

ABSTRACT

This study presents a novel modified thermal decomposition (MTD) technique for the synthesis of bulk $YBa_2Cu_3O_{7-\delta}$ (Y-123) ceramics with varying samarium oxide (Sm_2O_3) additions (0.0,0.1,0.3,0.5, 1.0 and 5.0 wt%) under ambient conditions. A structural analysis via X-ray diffraction (XRD) with Rietveld refinement confirmed the dominant formation of the orthorhombic Y-123 phase, accompanied by minor secondary phases, such as Y_2BaCuO_5 (Y-211) and $BaCuO_2$. Notably, at 0.1 wt% Sm_2O_3, a distinct $Sm_{1.15}Ba_{1.85}Cu_3O_7$ (Sm-123) phase emerged, contributing to enhanced phase stability and effective flux pinning. The optimized 0.1 wt% sample exhibited the highest oxygen content (~6.87), largest crystallite size (~1865 Å), and lowest lattice strain, factors directly linked to enhanced superconducting properties. Field emission scanning electron microscopy (FESEM) revealed significant grain growth (~8.14 μm) and enhanced grain connectivity at 0.1 wt%, while higher doping levels caused porosity and microstructural deterioration. High-resolution imaging further revealed zigzag grain boundaries and nanoscale inclusions acting as flux pinning centers. Energy-dispersive X-ray spectroscopy (EDX) confirmed the uniform elemental distribution and successful Sm incorporation. The 0.1 wt% Sm_2O_3-added sample achieved the highest critical current density ($J_c = 5.62$ kA/cm^2 at 77 K), with a narrow superconducting transition width ($\Delta T_c \approx 2.96$ K), a $T_{c\text{-onset}}$ of 92.21 K, and a $T_{c\text{-zero}}$ of 89.25 K, indicating minimal weak-link behavior. These findings demonstrate that low-level Sm_2O_3 addition effectively introduces flux pinning centers while preserving crystal integrity and oxygen stoichiometry. The resulting enhancement in superconducting performance underscores the scalability and efficacy of the MTD route for producing high-performance Y-123 ceramics.

1. Introduction

High-temperature superconductors (HTS), particularly $YBa_2Cu_3O_{7-\delta}$ (Y-123) have garnered significant attention due to their relatively high critical temperature (T_c), simple perovskite structure, and potential applications in power transmission, magnetic levitation, and magnetic resonance imaging [1,2]. Despite these advantages, the performance of Y-123 ceramic is often limited by weak intergranular coupling and low critical current density (J_c), particularly under applied magnetic fields [3–5]. These limitations are primarily attributed to grain boundary misalignments and poor flux pinning efficiency, which facilitate vortex motion and reduce current-carrying capacity [6–8]. To overcome these challenges, researchers have explored various strategies to improve microstructural uniformity and introduce artificial pinning centers that anchor vortices and thereby enhance J_c.

One promising strategy to overcome these challenges involves the incorporation of rare-earth oxides (REO), either through substitution or additive routes. Among these, samarium oxide (Sm_2O_3) has attracted

* Corresponding author.
E-mail address: mmak@upm.edu.my (M.M. Awang Kechik).

https://doi.org/10.1016/j.jmrt.2025.05.065
Received 7 April 2025; Received in revised form 8 May 2025; Accepted 8 May 2025
Available online 19 May 2025

interest for its dual role in structural stabilization and vortex pinning enhancement. The partial replacement of Sm^{3+} with Y^{3+}can induce beneficial lattice distortions and improve oxygen ordering along the Cu–O chains, thereby enhancing superconductivity [9–11]. Additionally, the addition of Sm_2O_3 may promote the in-situ formation of $SmBa_2Cu_3O_7$ (Sm-123) secondary phases, which serve as intrinsic flux pinning centers [12,13]. However, the effectiveness of REO doping depends strongly on the dopant concentration and synthesis route used, necessitating careful process optimization. For instance, Güdücü et al. (2024) showed that substituting terbium (Tb) at x = 0.01 enhanced the J_c by improving isotropic grain morphology despite a slight reduction in the T_c [14]. Similarly, Vojtkova et al. (2018) found that Sm_2O_3 microalloying, along with trace Yb contamination, refined the Y-211 particles and produced a secondary J_c peak under an applied magnetic field-an indication of enhanced pinning due to Sm-induced nano-defects [15]. Nonetheless, an excessive concentration of nano-Sm_2O_3 (>0.5 wt%) can degrade superconductivity by inducing porosity and reducing grain size, as shown by Aima (2018) [16]. This trend was echoed by Vojtkova (2018), who demonstrated that small additions of Sm_2O_3 or La_2O_3 refined Y-211 inclusions and improved the J_c when processed via top-seeded infiltration growth [11]. These findings highlight the need for a precise optimization of the REO content to balance the microstructural refinement and grain boundary integrity.

Alongside dopant optimization, the synthesis technique plays a pivotal role in determining phase purity, grain morphology, and oxygen incorporation in Y-123 ceramics [17–19]. Recently, a novel approach, termed the modified thermal decomposition (MTD) method, has emerged as a promising alternative to conventional approaches such as solid-state reaction (SSR), sol-gel (SG), thermal treatment (TT), and co-precipitation (COP) [20–23]. The MTD approach employs metal acetate precursors decomposed via a multi-stage thermal process that enables precise stoichiometric control and uniform ion dispersion at the atomic level. Unlike wet-chemical routes that require complex pH control, solvents, surfactants, or catalysts, the MTD technique relies solely on the controlled thermal breakdown of metal acetates, eliminating the need for polymeric binders (polyvinylpyrrolidone (PVP)), atmospheric regulation, or repeated grinding [19,24]. Compared to nitrate-based TT methods that may leave organic residues, the MTD method produces clean decomposition products and promotes uniform nucleation. These advantages contribute to enhanced microstructural integrity, improved oxygen incorporation, and better intergranular coupling, which are critical for stabilizing the orthorhombic phase and enhancing the J_c [24,25].

Previous studies have validated the effectiveness of the MTD method for fabricating high-performance Y-123 ceramics. Al-Gaashani et al. demonstrated that thermal decomposition strategies can yield high-purity CuO nanostructures in a single step without use of the catalysts or templates [25,26]. Building on this foundation, Arebat et al. and Sah et al. (2024) successfully adapted the MTD method for the synthesis of Y-123 ceramics, employing acetate-based precursors and tailored thermal treatment steps. Their findings confirmed that the MTD method offers enhanced phase formation, structural homogeneity, and improved superconducting properties compared to SSR and TT [17,19]. Complementary investigations by Yap et al. (2025) further validated the potential of this method, where a comparative analysis of synthesis techniques, including TT, SSR, and MTD, under ambient conditions showed that the MTD method yielded a Y-123 sample with the narrowest superconducting transition width (ΔT_c) and the highest phase purity (98.3 %) [27]. In a subsequent study, Arebat et al. (2025) expanded the MTD method by demonstrating its capability to produce high-T_c Y-123 ($T_{c\text{-onset}}$ = 93.72 K) using optimized thermal conditions, namely, calcination at 910 °C, sintering at 980 °C, and annealing in ambient air at 600 °C,thus eliminating the need for oxygen flow during processing [24]. This approach, supported by a TGA/DTG analysis, enabled gradual oxygen incorporation, reducing internal strain and improving the lattice stability. These parameters were adopted and refined in the present study, based on both the previous literature and the experience of in-house optimization [28]. The effectiveness of the MTD method has been validated through the optimal integration of REO. A recent study demonstrated that adding an ideal concentration of neodymium oxide (Nd_2O_3) to Y-123 led to better phase stability, enhanced grain size, and improved superconductivity performance [29]. In contrast, studies using conventional methods for REO addition frequently reported phase degradation, oxygen deficiencies, and reduced the T_c values [7,16,30].

Motivated by these findings, the current study explored the effects of various concentrations (0.0, 0.1, 0.3, 0.5, 1.0, and 5.0 wt%) of Sm_2O_3 on the microstructure and superconductivity of bulk Y-123 ceramics synthesized via the MTD method. Sm_2O_3 was selected due to its favorable ionic size, minimal lattice mismatch, and well-documented effectiveness in enhancing flux pinning and phase stability [11,12]. The chosen range of concentrations enabled a comparative evaluation of both the beneficial and adverse effects, where low levels (≤0.5 wt%) of Sm_2O_3 were expected to enhance flux pinning and grain connectivity and higher levels (>1.0 wt%) to induce structural disorder, phase decomposition, and grain boundary degradation [11,16]. Although addition of REO has been widely studied in Y-123 systems prepared by conventional methods [29–32],while the MTD approach has independently demonstrated significant advantages in phase control and grain refinement, the combined application of Sm_2O_3 doping within the MTD framework remains unaddressed in the literature. This study addressed that gap by providing a comprehensive, concentration-dependent analysis of the addition of Sm_2O_3 using the MTD route that links processing parameters, phase evolution, and superconductivity. This novel integration of Sm_2O_3 with the MTD method established new process–structure–property relationships, offering fresh insights into REO-based performance tuning in high-T_c superconducting ceramics.

For clarity and consistency, all the abbreviations and key technical terms utilized throughout this manuscript are summarized in Table 1.

2. Materials and methods section

2.1. Preparation process

Bulk $YBa_2Cu_3O_{7-\delta}$ (Y-123) ceramics were synthesized using the MTD method, following the procedures adapted from Arebat et al. [24,28]. High-purity precursors-yttrium acetate ($Y(CH_3COO)_3{\cdot}4H_2O$), barium acetate ($Ba(CH_3COO)_2$), and copper acetate ($Cu(CH_3COO)_2$) (≥99.9 % purity, Alfa Aesar), were weighed in stoichiometric proportions. The weighed precursors were manually mixed for 15 min in a crucible using a clean glass rod to ensure initial homogeneity. The mixture underwent pre-calcination at 600 °C for 30 min to eliminate volatile components. The pre-calcined powder was then ground for an additional 30 min using a mortar to enhance homogeneity. The resulting powder was transferred to an alumina boat and subjected to calcination at 910 °C for 24 h. The powder was ground again for 15 min post-calcination to achieve a consistent particle size distribution before it was formed into pellets.

Samarium oxide (Sm_2O_3) was incorporated into the Y-123 precursor matrix at concentrations of 0.1, 0.3, 0.5, 1.0, and 5.0 wt%, followed by thorough grinding to ensure uniform dispersion. The resulting powders were uniaxially pressed into cylindrical pellets (~11.5 mm diameter × ~1.7 mm thickness) using a manual hydraulic press. Sintering was performed at 980 °C for 24 h under ambient atmospheric conditions, followed by slow cooling to 600 °C and holding for 12 h to promote

Table 1
Nomenclature and abbreviations used in the manuscript.

Symbol/Abbreviation	Definition	Symbol/Abbreviation	Definition
MTD	Modified thermal decomposition	ΔT_c	Width of the resistive transition
SSR	Solid-state reaction	MRI	Magnetic resonance imaging
TT	Thermal treatment	Nd_2O_3	Neodymium oxide
SG	Sol–Gel	Sm_2O_3	Samarium oxide
COP	Co-precipitation	REO	Rare-earth oxide
PVP	Polyvinylpyrrolidone	$Y(CH_3COO)_3{\cdot}4H_2O$	Yttrium acetate
K	Kelvin (unit of temperature)	Ba $(CH_3COO)_2$	Barium acetate
A	Ampere (unit of current)	Cu $(CH_3COO)_2$	Copper acetate
cm	Centimeter	YBCO	Yttrium–barium–copper–oxygen
Y-123	$YBa_2Cu_3O_{7-\delta}$ ceramic	*a*, *b*, *c*	Lattice parameters (axes of the unit cell)
Y-211	Y_2BaCuO_5 secondary phase	7−δ	Oxygen content in YBCO structure
$BaCuO_2$	Barium copper oxide	L	Crystallite size
Sm-123	$Sm_{1.15}Ba_{1.85}Cu_3O_7$ superconducting phase	λ	X-ray wavelength
XRD	X-ray diffraction	β	Full width at half maximum (FWHM) of the diffraction peak
EDX	Energy-dispersive X-ray spectroscopy	θ	Bragg angle
4 PP	Four-point probe	V	Voltage
SQUID	Superconducting quantum interference Device	I	Applied current
FESEM	Field emission scanning electron Microscope	R	Resistance
J_c	Critical current density	*p*	Hole carrier concentration
T_c	Critical temperature	T_c^{Max}	Highest superconducting transition temperature
$T_{c\text{-onset}}$	Start of the superconducting transition	Δm	Difference in magnetic moment
$T_{c\text{-zero}}$	Temperature at which zero resistance is achieved	ICSD	Inorganic crystal structure Database

gradual oxygen diffusion. The selected thermal profile was based on previous studies demonstrating its effectiveness in enhancing phase stability and oxygen incorporation in Y-123 ceramics [24,28].

To prevent environmental interference, all the synthesis steps, including precursor handling, grinding, mixing, and pelletizing, were conducted in a climate-controlled laboratory. Temperature and relative humidity were continuously monitored using a calibrated Hubstein HTC-1 thermohygrometer, which recorded a stable environment of 25 ± 1 °C and 51 ± 5 % relative humidity [33–35]. These conditions were maintained throughout the experimental procedure to minimize moisture absorption by hygroscopic acetate-based precursors and to ensure reproducibility and phase integrity. Following sintering, all samples were stored in sealed desiccators until further characterization.

A step-by-step flowchart summarizing the complete experimental

Table 2
Chemical specifications of starting materials used in the sample synthesis.

Material Name	Chemical Formula	Purity (%)	Supplier	Physical Form
Yttrium acetate	$Y(CH_3COO)_3{\cdot}4H_2O$	≥99.9 %	Alfa Aesar	Powder
Barium acetate	Ba $(CH_3COO)_2$	≥99.9 %	Alfa Aesar	Powder
Copper acetate	Cu $(CH_3COO)_2{\cdot}H_2O$	≥99.9 %	Alfa Aesar	Powder
Samarium oxide	Sm_2O_3	≥99.9 %	Sigma-Aldrich	Powder

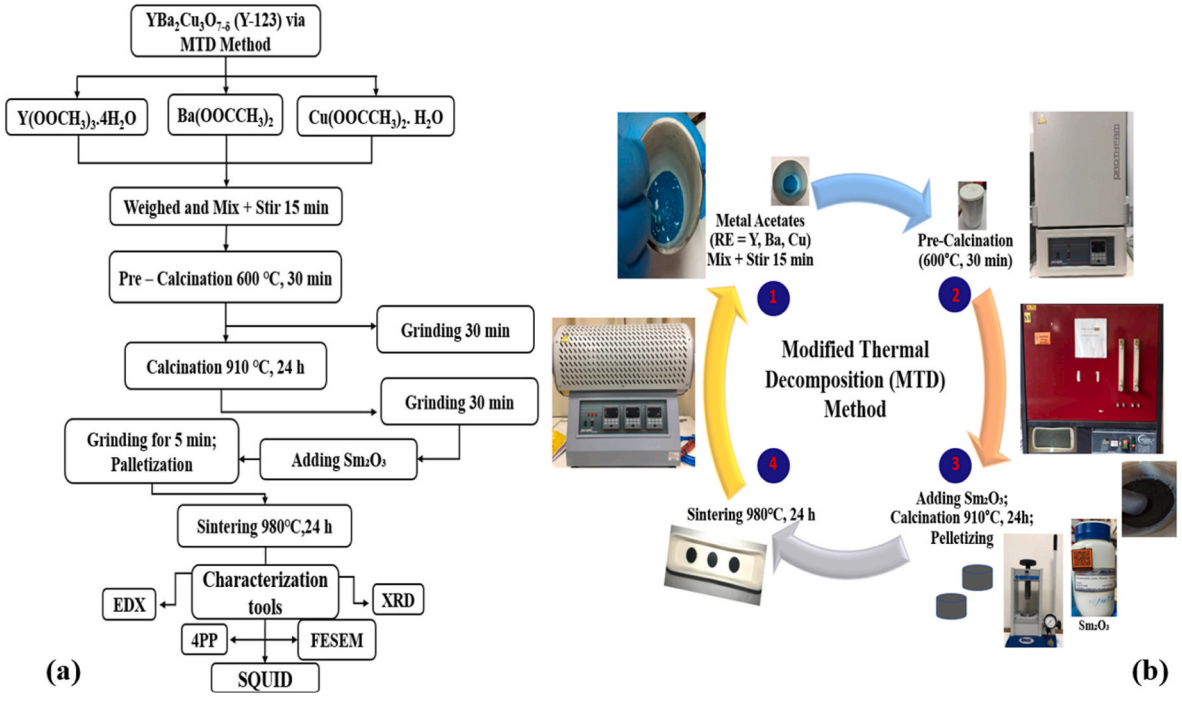

Fig. 1. **(a)** Flowchart illustrating the synthesis and characterization procedures for Sm_2O_3-added Y-123 ceramics via MTD method; **(b)** Schematic representation of the experimental specimen preparation process.

workflow is provided in Fig. 1a and 1b presents photographs of the tools and instruments used during the synthesis. A summary of the chemical composition, purity, and suppliers of all the starting materials is given in Table 2.

2.2. Characterization tools

The phase composition and crystal structure of the samples were analyzed using X-ray diffraction (XRD) with Cu-Kα radiation (λ = 1.54 Å) on a PW 3040/60 MPD X'Pert PRO diffractometer (Panalytical Philips DY 1861). Surface morphology and elemental composition were examined using field emission scanning electron microscopy (FESEM) coupled with energy-dispersive X-ray spectroscopy (EDX). The superconducting transition temperature (T_c) was determined using the four-probe technique with a Keithley 6221 DC Current Source and a Keithley 2182A Nanovoltmeter in a closed-cycle helium cryostat, covering a temperature range of 30–300 K. The critical current density J_c was evaluated using a Quantum Design MPMS5 SQUID magnetometer under zero-field-cooled conditions at 77 K with an applied magnetic field of 1 Oe. Magnetization hysteresis (M − H) loops were recorded in applied magnetic fields ranging from 0 to +5 T at 20 K. The J_c of the samples (dimensions ~1.5 mm × 1.5 mm × 0.5 mm) was calculated using the extended Bean critical state model [36]:

$$J_c = \frac{20\Delta m}{a^2 d\left(b - \frac{a}{3}\right)} \quad (1)$$

where d is the sample's thickness; a, b ($a < b$) are the cross-sectional dimensions of a rectangular sample; and Δm (in emu units, 1 emu = 10^{-3} A m^2) is the M − H loop's width.

To support reproducibility and transparency, Fig. 2a–d presents photographs of all physical instruments used in this study, while Fig. 3a–c includes screenshots of the software platforms employed for data processing and visualization, namely X'Pert HighScore Plus for XRD analysis, OriginPro 2019 for graphical plotting, and ImageJ for grain size quantification.

3. Results and discussions

3.1. X-ray diffraction (XRD) analysis

Fig. 4a and b presents the XRD patterns of the bulk $YBa_2Cu_3O_{7-\delta}$ (Y-123) samples to which various concentrations (0.0–5.0 wt%) of Sm_2O_3 had been added under ambient annealing conditions. The diffraction patterns were dominated by the characteristic peaks of the orthorhombic Y-123 phase (space group *Pmmm*, ICSD: 98–003–1706), with strong reflections observed at $2\theta \approx 32.4^\circ$ and 32.8°, corresponding to the (013) and (103) crystallographic planes, respectively. Phase identification and refinement were carried out using the X'Pert HighScore Plus software with Rietveld refinement and ICSD reference standards [24,27]. All the compositions retained the orthorhombic perovskite structure, confirming successful phase formation of Y-123 across the Sm_2O_3 doping range.

At a lower concentration of Sm_2O_3 (0.1 wt%), minor secondary phases were identified, including $Sm_{1.15}Ba_{1.85}Cu_3O_7$ (Sm-123) (ICSD: 98–002–5671), alongside Y_2BaCuO_5 (Y-211) (ICSD: 98–002–4901) and $BaCuO_2$ (ICSD: 98–002–5028), consistent with previous research [2,24]. As the Sm_2O_3 concentration was increased, particularly beyond 0.5 wt %, these secondary phases became more pronounced, as evidenced by the increased intensity of their diffraction peaks [11,16]. Although achieving complete phase purity in REO-added systems remains a challenge, the presence of finely dispersed Y-211 and Sm-123 particles may enhance flux pinning, especially when confined to nanoscale domains. Importantly, despite the emergence of these secondary phases, all samples maintained an orthorhombic crystal structure-critical for preserving high T_c values and ensuring effective intergranular superconducting pathways [15,30,37].

Tables 3 and 4 summarize the evolution of the structural parameters of specimens, revealing key insights into the observed enhancements in superconducting properties. At a concentration of 0.1 wt%, the Sm-123

Fig. 2. Photographic representation of physical instruments used in this study: **(a)** X-ray diffraction (XRD); **(b)** FESEM-EDX system; **(c)** four-point probe (4 PP); (d) SQUID magnetometer.

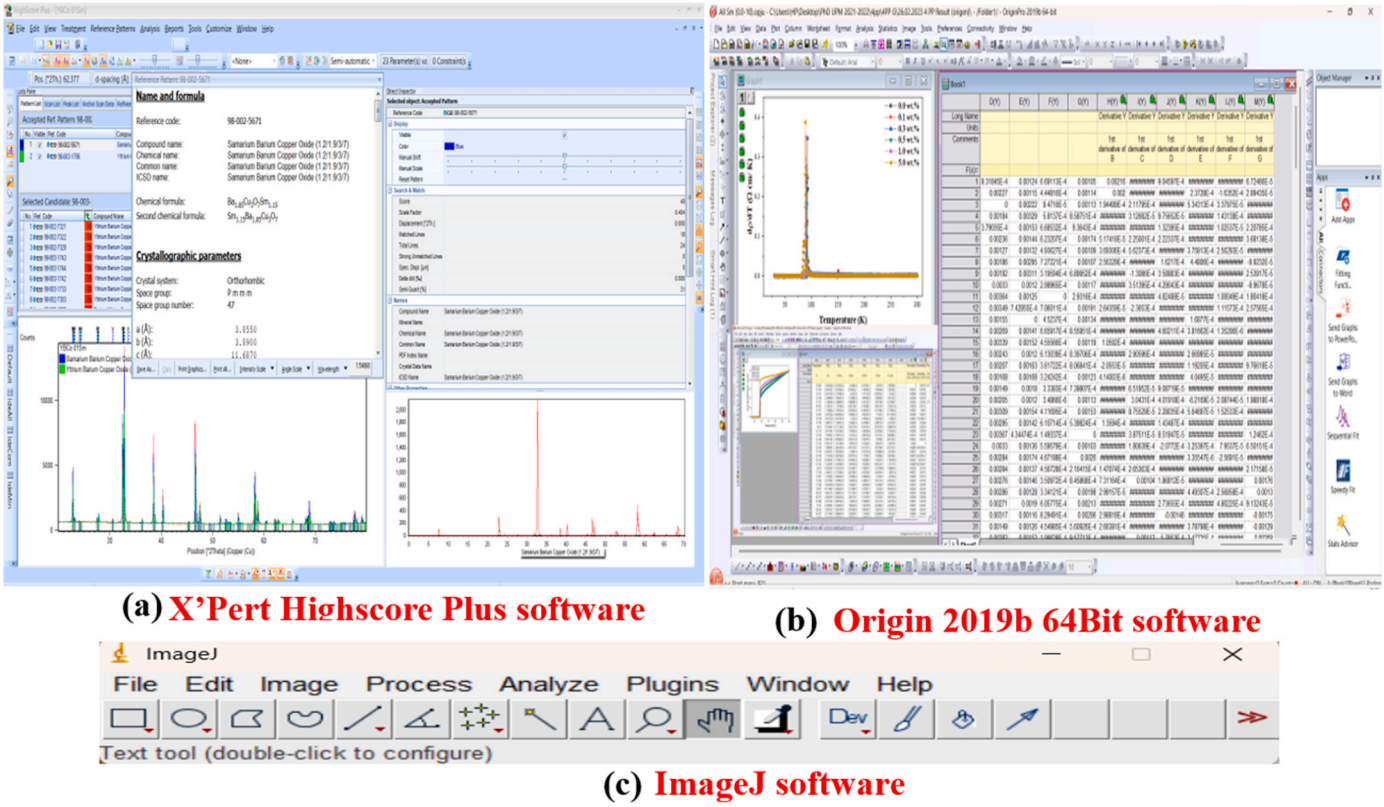

Fig. 3. Screenshots of the software tools used for data analysis and interpretation: **(a)** X'Pert HighScore Plus; **(b)** OriginPro 2019; **(c)** ImageJ.

phase volume fraction reached a maximum of 2.7 %, indicating a favorable partial substitution of Sm^{3+} for Y^{3+}, owing to their similar ionic radii [38,39]. This substitution preserved the orthorhombic symmetry and promoted improved oxygen ordering along the Cu–O chains, facilitating more efficient charge carrier transport [11,40]. The same sample also exhibited peak shifts toward lower 2θ values (Fig. 4b), suggesting slight lattice expansion and improved crystallinity. These changes are typically associated with reduced internal strain, increased oxygen uptake, and enhanced phase coherence [9,37]. Such structural modifications are consistent with enhanced oxygen alignment within the Cu–O chains, which is known to support higher carrier mobility and stronger superconducting behavior. Fig. 5 illustrates the correlation between the undoped and optimally doped samples (0.1 wt%) in terms of oxygen content, crystallite size, and lattice strain. The results show that the 0.1 wt% sample exhibited higher values for oxygen content and crystallite size, while maintaining lower lattice strain—all of which contribute synergistically to improved superconducting performance [11,13,39].

The orthorhombicity of the Y-123 structure, calculated as (b–a)/ (b + a), decreased progressively with increasing Sm_2O_3 content, as detailed in Table 3. This reduction in lattice distortion was attributed to the cumulative structural strain and oxygen site disorder, both of which are known to suppress the T_c [7,16]. The oxygen content (7-δ) was estimated using the formula [41]:

$$7 - \delta = 75.25 - 5.856c \tag{2}$$

where, c is the lattice's parameter along the c-axis. The 0.1 wt% Sm_2O_3-doped sample exhibited a slight increase in oxygen content (~6.87), indicating enhanced oxygen ordering with full occupancy at the O(1) sites along the b-axis in the CuO chains [32]. Furthermore, the crystallite size (L) was calculated using the Debye–Scherrer equation [42]:

$$L = \frac{K\lambda}{\beta \cos\theta} \tag{3}$$

where k = (0.9) is the shape factor, λ = 0.1542 nm is the X-ray's wavelength, β is the full width at half maximum (FWHM), and θ is the Bragg angle.

As shown in Table 4, crystallite size (L) increased initially with the Sm_2O_3 concentrations, reaching a maximum of 1865 Å at 0.1 wt%, before decreasing at higher doping levels. This trend suggested that the formation of a modest amount of the Sm-123 phase promoted local grain growth and stabilized the Y-123 matrix, whereas excessive concentration of Sm_2O_3 (>1.0 wt%) introduced structural disruptions, hindered grain coarsening, and contributed to crystallite fragmentation [37]. Thus, a concentration of 0.1 wt% of Sm_2O_3 represented the ideal doping level, effectively balancing phase composition, lattice integrity, and grain connectivity to maximize superconductivity.

At higher doping levels (≥1.0 wt%), the Sm-123 vol fraction diminished while undesirable secondary phases such as Y-211 (3.1 %) and $BaCuO_2$ (3.5 %) became dominant. This phase imbalance led to peak broadening and a shift toward higher 2θ values in the XRD patterns (Fig. 4b), indicative of lattice contraction and elevated microstrain. Such structural degradation is attributed to increased porosity, oxygen deficiency, and grain boundary deterioration, factors that disrupt superconducting pathways. These findings underscore the inherent challenge of achieving complete phase purity in rare-earth-doped Y-123 systems, particularly at elevated doping concentrations [43,44]. Interestingly, analogous microstructural destabilization has been observed in thermally treated P91B steels, where excessive heat exposure induces secondary phase formation and lattice distortion, ultimately degrading material performance [45]. These cross-material parallels further highlight the importance of carefully controlling dopant levels and thermal processing to preserve phase stability and microstructural

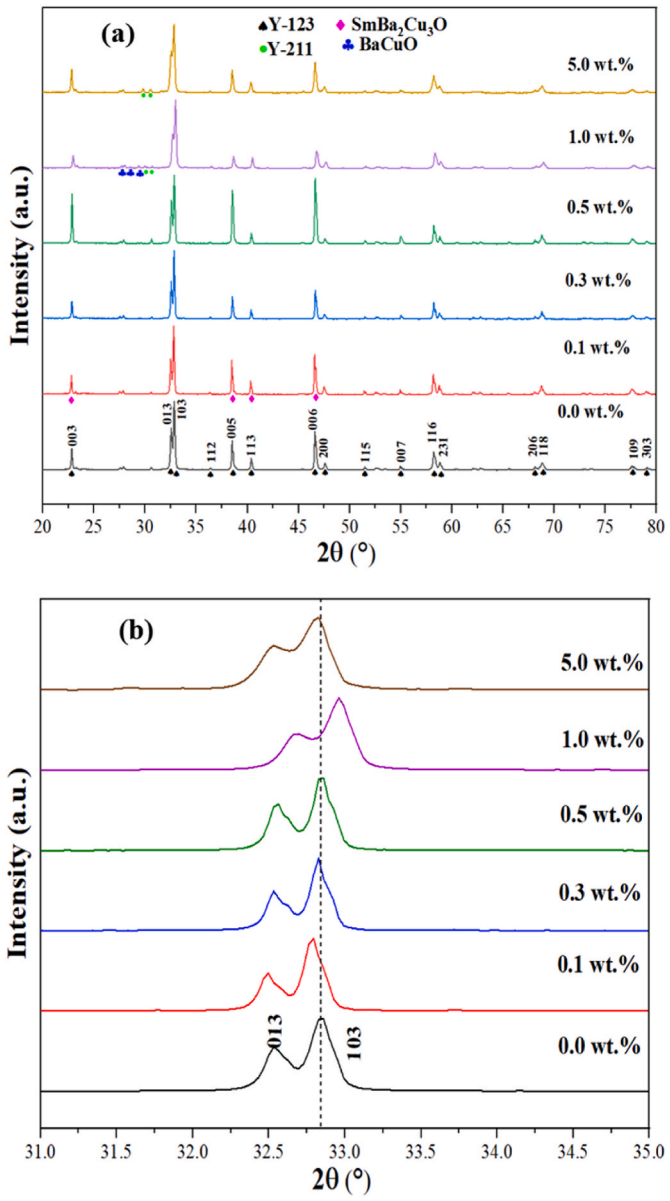

Fig. 4. **(a)** XRD patterns of bulk Y-123 samples with varying Sm_2O_3 concentrations; **(b)** Magnified XRD patterns highlighting the (013) and (103) diffraction peaks.

Table 3
Lattice parameters, oxygen content, and orthorhombicity of bulk Y-123 ceramics with varying Sm_2O_3 concentrations.

Sm_2O_3 Addition wt. %	Lattice Parameters (Å)			Orthorhombicity (Å)	$O_{7-\delta}$
	a-axis	*b*-axis	*c*-axis	| (b-a)/(a+b) |	
0.0	3.820	3.885	11.683	0.00844	6.834
0.1	3.825	3.889	11.676	0.00827	6.873
0.3	3.822	3.887	11.681	0.00841	6.850
0.5	3.824	3.888	11.683	0.00830	6.834
1.0	3.826	3.886	11.684	0.00788	6.830
5.0	3.825	3.887	11.679	0.00801	6.858

integrity. In summary, the XRD analysis confirms that 0.1 wt% Sm_2O_3 yields an optimal balance of orthorhombic phase stability, oxygen ordering, and crystallite growth-structural features that underpin the enhanced flux pinning and intergranular coupling observed in later superconducting transport measurements.

3.2. Field emission scanning electron microscopy (FESEM) analysis

Microstructural refinement plays a pivotal role in determining the superconducting properties of Y-123 ceramics, particularly by influencing magnetic flux pinning and intergranular current transport [46,47]. In superconducting materials, intentional microstructural tuning, such as the introduction of the controlled defects or grain boundary engineering, has been shown to enhance flux pinning effectiveness and promote stable current pathways [2,14,48]. However, the success of such modifications strongly depends on parameters like grain size, morphology, and distribution. Well-connected, uniformly distributed grains tend to reduce weak-link behavior and promote more coherent charge transport across grain boundaries [17,49]. Recent findings by Arebat et al. (2025) demonstrated that the MTD method, especially under ambient annealing conditions, facilitates oxygen incorporation into the Y-123 lattice while minimizing the formation of structural defects [28]. These samples showed clean, rectangular grain morphologies and a highly aligned granular architecture, which is beneficial for sustaining strong intergranular coupling. The current study builds upon these findings and links them to the structural observations discussed in Section 3.1 (XRD Analysis), particularly the optimized crystallinity, reduced lattice strain, and enhanced oxygen ordering observed at 0.1 wt % Sm_2O_3. These structural advantages are now examined further in terms of their manifestation in the grain-scale and nanoscale features visualized by FESEM.

Fig. 6 presents the FESEM micrographs alongside corresponding EDX spectra of Y-123 ceramics synthesized via the MTD method with Sm_2O_3 concentrations ranging from 0.0 to 5.0 wt%. Grain size evaluations were conducted using ImageJ software, to analyze 100 randomly selected elongated grains per sample [50,51]. The findings are summarized in Table 5. The undoped Y-123 sample exhibited moderately sized grains with noticeable porosity and limited intergranular cohesion, features typically associated with suboptimal flux pinning and weaker superconducting pathways. In contrast, the 0.1 wt% Sm_2O_3-doped sample exhibited the largest average grain size (~8.14 μm), which was attributed to the enhanced grain boundary diffusion and improved densification. This behavior was likely driven by the minor substitution of Sm^{3+} ions for Y^{3+}, which introduced localized strain fields that promoted grain growth while preserving lattice stability, consistent with earlier reports [16,19,52].

At higher Sm_2O_3 concentrations (≥0.3 wt%), a progressive reduction in grain size was observed, culminating in an average grain size of approximately 2.49 μm at doping level of 5.0 wt%. This grain refinement was accompanied by increased porosity, the emergence of secondary phases, notably Y-211 and $BaCuO_2$, and a deterioration of grain boundary integrity. The FESEM imaging revealed irregular grain morphologies and disrupted intergranular contacts at elevated Sm_2O_3 levels, leading to the formation of insulating barriers that obstructed coherent charge carrier transport across the superconducting matrix. These microstructural degradations correlated strongly with the XRD findings, which showed intensified secondary phase peaks and diffraction peak shifts indicative of lattice contraction and oxygen disorder. Interestingly, similar degradation mechanisms were reported by Khajuria et al. (2024) in the heat-affected zones of structural steels, where excessive thermal exposure led to the weakening of grain boundaries, porosity, and mechanical deterioration [53,54]. Such cross-disciplinary parallels underscore the universal importance of microstructural stability in preserving mechanical and electronic performance. Collectively, these observations affirmed that the excessive addition of Sm_2O_3 compromised the structural uniformity of the Y-123 phase, destabilizing grain boundary networks and significantly degrading superconducting pathways and the J_c. These results aligned closely with earlier reports, which emphasized that REO overload leads to structural fragmentation,

Table 4
Structural characterization parameters of bulk Y-123 ceramics with different Sm_2O_3 additions.

Sm_2O_3 Addition wt.%	Volume fraction %				Volume of Unit Cell	Crystallite Size (L)	Lattice Strain
	Y-123	Sm-123	Y-211	$BaCuO_2$	V^3 (Å)	Y-123(Å)	Y-123 %
0.0	100	/	/	/	173.41	1438	0.142
0.1	97.3	2.7	/	/	173.66	1865	0.118
0.3	100	/	/	/	173.52	1820	0.120
0.5	100	/	/	/	173.68	1531	0.135
1.0	93.4	/	3.1	3.5	173.71	743.0	0.228
5.0	94.3	/	5.7	/	173.66	682.0	0.243

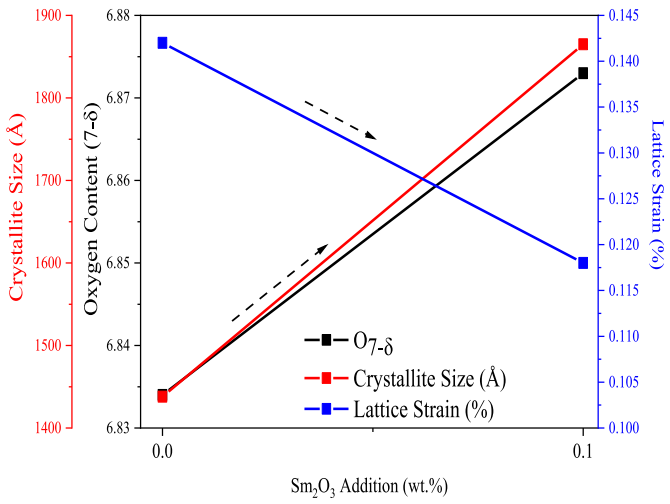

Fig. 5. Correlation of oxygen content (7–δ), crystallite size (L), and lattice strain between the pure Y-123 sample and the optimal 0.1 wt% Sm_2O_3-added Y-123 sample.

weakens intergranular coupling, and suppresses superconductivity [12,55].

To systematically characterize the microstructural changes across multiple length scales, high-resolution cross-sectional FESEM imaging was conducted at low, medium, and high magnifications on the optimal (0.1 wt%) sample, as depicted in Fig. 7a–c. The cross-sectional micrographs revealed a densely packed microstructure characterized by reduced porosity, uniform grain distribution, and strong intergranular cohesion. These features confirm that the MTD method, combined with the controlled addition, of Sm_2O_3 promoted phase homogeneity and refined the microstructural integrity. Such a compact granular architecture is critical for minimizing weak links at grain boundaries, thereby enhancing superconducting pathways and improving the critical transport of current.

At low magnification (5000 × , Fig. 7a), the FESEM image revealed a densely packed granular microstructure characterized by well-connected grains and negligible porosity. This compact morphology suggested that the MTD method, combined with the addition of optimized 0.1 wt% Sm_2O_3, effectively promoted uniform grain growth and minimized weak links at the grain boundaries. Such densely packed grains enhanced intergranular coupling, reduced flux flow barriers, and facilitated continuous superconducting current pathways throughout the Y-123 matrix. The observed structural uniformity at this scale directly supported the improved superconducting transport properties achieved in the optimized sample [27].

At medium magnification (15,000 × , Fig. 7b), the FESEM micrograph reveals the emergence of nanoscale features along grain boundaries, indicative of high phase purity and refined microstructural control. These nano-entities, uniformly distributed across the grain junctions, likely act as effective flux pinning centers by anchoring vortices and restricting their motion under an applied magnetic field. The presence of these finely dispersed secondary structures enhances overall phase stability and strengthens the homogeneity of the superconducting matrix. Furthermore, the organized nanoscale architecture suggests that 0.1 wt% Sm_2O_3 doping not only facilitates grain growth but also promotes controlled formation of secondary pinning phases, reinforcing vortex immobilization and boosting the critical current density (J_c) [16,50].

At high magnification (50,000 × , Fig. 7c), the FESEM micrograph distinctly revealed a zigzag grain morphology, accompanied by nano-sized entities embedded within the grain boundaries. This characteristic zigzag crystallization pattern reflected a highly controlled grain growth enabled by the MTD synthesis method and optimal Sm_2O_3 doping. Such a textured grain boundary network enhanced grain interconnectivity and created multiple effective flux pinning landscapes, critical for impeding vortex motion. The embedded nano-features further act as localized pinning centers, minimizing flux creep and stabilizing superconducting currents under applied magnetic fields. The coexistence of an optimized grain morphology and finely distributed nanoscale defects at 0.1 wt% Sm_2O_3 underscored the ideal doping level, achieving a synergistic balance between phase integrity, vortex immobilization, and enhanced superconducting transport properties [2,5].

Further structural confirmation was obtained through the EDX elemental mapping of the 0.1 wt% Sm_2O_3 sample (Fig. 8), which revealed a uniform distribution of Y, Ba, Cu, and O, along with homogeneously incorporated Sm, without evidence of significant clustering. These results, which were consistent with the XRD analysis (Table 2), confirmed the successful integration of Sm_2O_3 into the Y-123 lattice. The absence of phase segregation suggested that the synthesis process had effectively facilitated the incorporation of Sm_2O_3, ensuring a well-distributed chemical composition. This optimized microstructure was crucial for maintaining structural integrity, improving flux pinning efficiency, and enhancing the overall superconductivity. Fig. 9 illustrates the relationship between grain size and Sm_2O_3 concentration. At higher Sm_2O_3 concentrations (≥5.0 wt%), a significant increase in porosity and irregular grain morphology was observed. These microstructural changes led to a less interconnected grain structure, disrupted charge carrier pathways, and diminished superconducting efficiency. Excessive Sm_2O_3 doping introduced non-uniform grain boundaries, creating weak links that impeded the coherent superconducting transport. These observations reaffirmed the detrimental impact of the addition of excessive amounts of REO on the microstructural stability and superconducting performance of Y-123 ceramics. Collectively, the results demonstrated that the MTD method, combined with 0.1 wt% Sm_2O_3 addition, effectively refined the Y-123 microstructure, promoting densification, intergranular coupling, and enhanced flux pinning. This study highlighted the critical importance of precise control over grain morphology and nanoscale defect structures in achieving high-performance superconducting ceramics suitable for advanced technological applications.

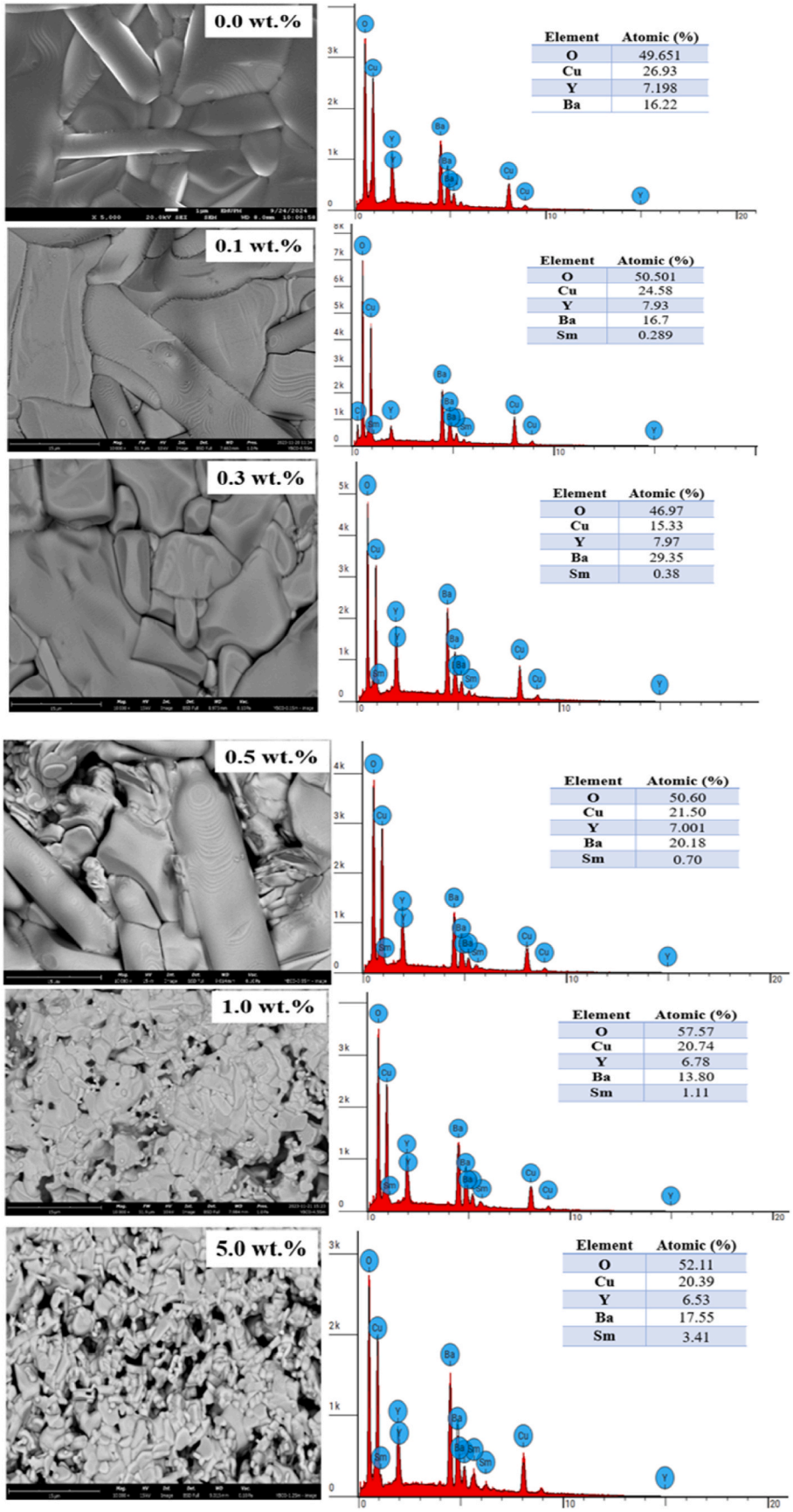

Fig. 6. SEM micrographs (left) and corresponding EDX spectra (right) along with chemical composition of Y-123 samples synthesized with varying concentrations of Sm_2O_3 addition.

Table 5
Average grain sizes of bulk Y-123 ceramics synthesized with different Sm_2O_3 additions.

Sm_2O_3 Addition wt.%	0.0	0.1	0.3	0.5	1.0	5.0
Average grain Sizes (μm)	~6.56 ±0.58	~8.14 ±0.65	~6.55 ±0.37	~5.96 ±0.49	~3.01 ±0.11	~2.49 ±0.09

3.3. Superconductive characteristics

3.3.1. Critical current density (J_c)analysis

The incorporation of REO elements into the Y-123 superconductor matrix has been widely demonstrated to enhance vortex stabilization, significantly improving the J_c. This enhancement is primarily attributed to effective flux pinning, which plays a crucial role in maintaining superconductivity under applied magnetic fields [56,57]. Additionally, the synthesis method is a key determinant in optimizing superconducting properties, as it influences grain connectivity, defect distribution, and secondary phase formation. In this study, Sm_2O_3 was introduced as a doping element, and its effects on J_c were thoroughly investigated using the MTD method. The dimensions of the samples were prepared as specified in Section 2.2. Fig. 10 presents the J_c values for the pure Y-123 sample and Sm_2O_3-added samples at concentrations of 0.1, 0.5, and 5.0 wt%, which were measured as 2.36, 5.62, 1.98, and 1.20 kA/cm^2, respectively.

The addition of 0.1 wt% Sm_2O_3 resulted in a remarkable enhancement, where the J_c of the pure sample more than doubled. This improvement was attributed to the optimized flux-pinning centers, which effectively anchored the magnetic vortices without significantly disrupting the Y-123 matrix. A secondary peak effect was observed in the J_c(B) curves, with J_c reaching 1.66 kA/cm^2 at 0.90 T, suggesting an additional flux pinning mechanism that was likely related to a localized oxygen deficiency-induced disorder [11,15,58,59]. Such secondary peak behavior has similarly been reported in (Sm, Eu, Gd) $Ba_2Cu_3O_{7-\delta}$ and (Nd, Eu, Gd) $Ba_2Cu_3O_{7-\delta}$ superconductors by Agarwal et al. and Miryala et al. [12,60]. In contrast, increasing the Sm_2O_3 content to 0.5 and 5.0 wt% resulted in a decline in the J_c. This reduction was attributed to the excessive formation of larger secondary phase particles, which acted as ineffective flux-pinning sites, introducing lattice strain, and disrupting intergranular connectivity, ultimately weakening the superconducting pathways. These results were in line with the XRD findings, which indicated an increased fraction of secondary phases and structural

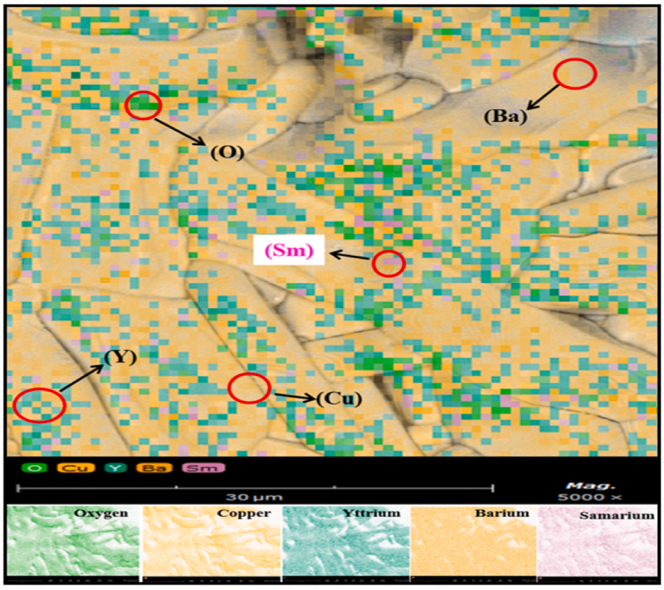

Fig. 8. Elemental distribution mapping in Y-123 superconductors of the optimal 0.1 wt% Sm_2O_3-added Y-123 sample.

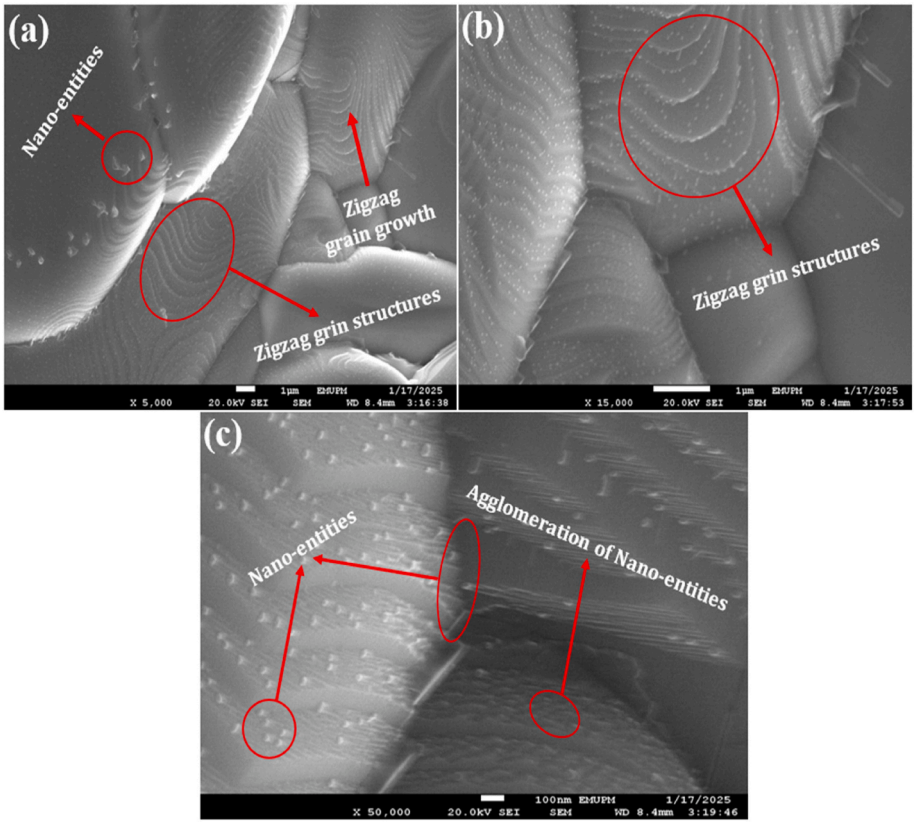

Fig. 7. (a–c). High-resolution cross-sectional FESEM micrographs of the optimal 0.1 wt% Sm_2O_3-added Y-123 ceramic sample at different magnifications.

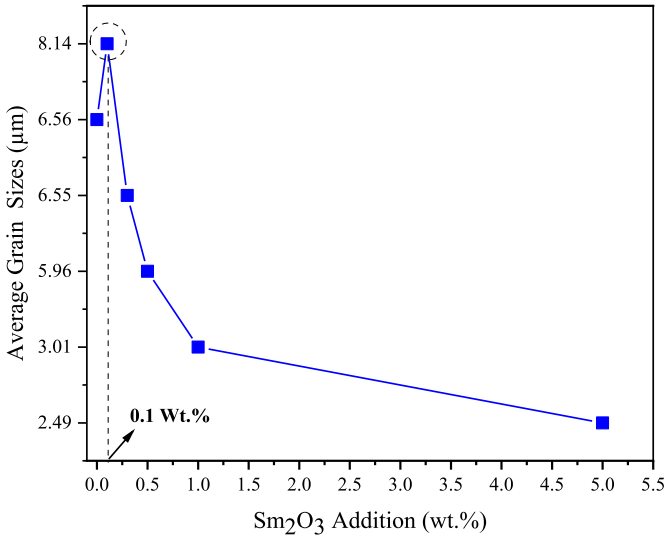

Fig. 9. Correlation between Sm_2O_3 concentration (0.0–5.0 wt%) and average grain size in Y-123 ceramics.

distortion at higher Sm_2O_3 concentrations (Table 4).

A comparison with previously reported wet chemical synthesis methods [2,50] highlighted that the pure Y-123 sample synthesized via the MTD method exhibited a notably higher J_c, further emphasizing the superior microstructural refinement achieved through this route. Fig. 11 illustrates the relationship between the Sm_2O_3 concentration (0.0, 0.1, 0.5, and 5.0 wt%) and J_c, further substantiating that 0.1 wt% was the optimal doping level for maximizing the J_c in Y-123 superconductors synthesized using the MTD method. The highest J_c observed in the 0.1 wt% Sm_2O_3 sample was attributed to the formation of nanoscale Sm-123 secondary phase particles, which functioned as efficient vortex pinning centers, a mechanism corroborated by prior studies [5,55]. At the same time, there was minimal disruption to the Y-123 matrix, thus ensuring enhanced flux pinning and improved superconducting pathways. Conversely, at higher doping levels (0.5 and 5.0 wt%), a decline in J_c was observed, which could be attributed to the formation of larger, ineffective secondary phase particles and increased lattice strain, consistent with previous reports [16]. These structural degradations

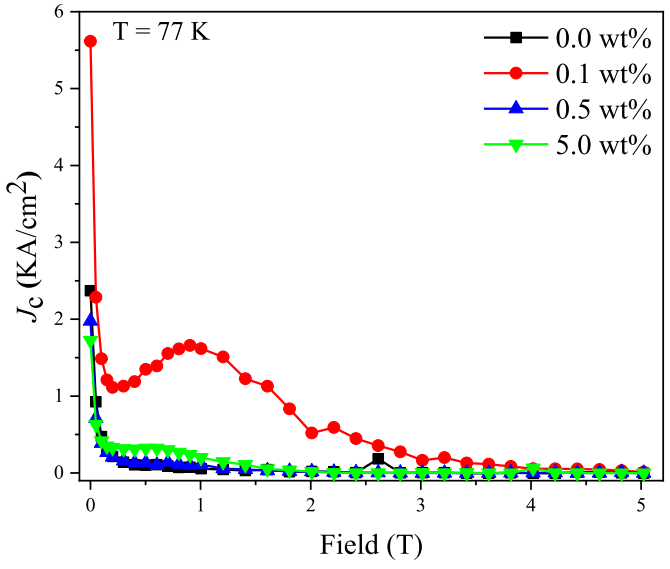

Fig. 10. Variation of critical current density (J_c) versus applied magnetic field at 77 K for selected Y-123 samples (pure, 0.1 wt%, 0.5 wt%, and 5.0 wt % Sm_2O_3).

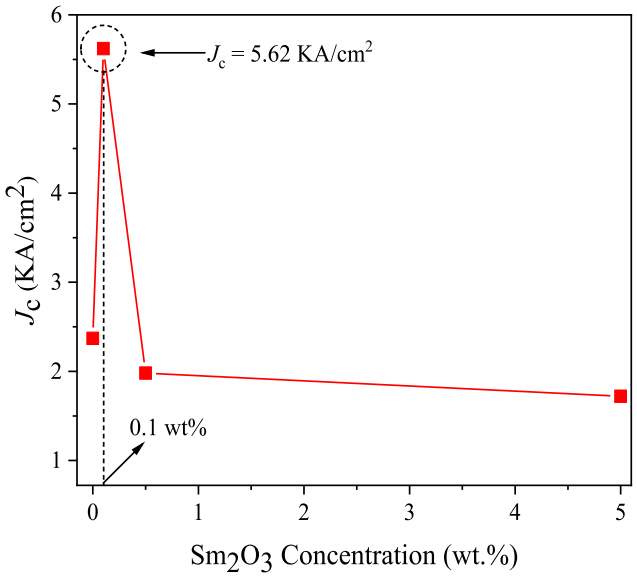

Fig. 11. Correlation between Sm_2O_3 concentration (0.1, 0.5, and 5.0 wt%) and critical current density (J_c) in Y-123 ceramics.

reduced the vortex pinning efficiency and disrupted the superconducting pathways. This behavior was in parallels with the phenomena observed in structural steels, where microstructural coarsening and grain boundary deterioration resulting from welding or thermal treatments, have been shown to compromise mechanical strength and fracture resistance [61,62]. Similarly, maintaining the fine, stable microstructural features in the Y-123 ceramics was essential for optimizing flux pinning and preserving high critical current densities. These results highlighted the critical importance of precise doping control and microstructural engineering in superconductor optimization, reinforcing that even small deviations in the secondary phase distribution can have a profound impact on superconductivity.

3.3.2. *Electrical resistivity measurements*

Fig. 12a and b presents the normalized resistivity of bulk the Y-123 samples with various Sm_2O_3 concentrations (0.0–5.0 wt%) as a function of temperature. The four-point probe (4 PP) instrument was employed to measure resistivity across the 30–300 K range [24]. The experimental setup, illustrated in Fig. 14, consisted of (a) a schematic representation of the measurement configuration, and (b) a photograph of the sample holder [29]. In this setup, the current was applied through the outer probes, and voltage is recorded across the inner probes. The resistance was calculated according to Ohm's Law ($R=V/I$), where V represents the measured voltage and I the applied current. All the measurements were conducted using a helium-cooled cryogenic system, while the samples were gradually heated from their minimum temperature. The T_c was determined from the temperature-resistance profiles. As shown in Fig. 12a, all the samples exhibited metallic behavior in the normal state up to $T_{c\text{-onset}}$. Notably, except for the 5.0 wt% Sm_2O_3-added sample, all the other compositions displayed single-step transitions in their resistivity curves, indicating a predominant Y-123 phase formation with strong intergranular connectivity (Figure, 12b), consistent with the XRD results and summarized in Table 4 [46]. To further refine the determination of the $T_{c\text{-onset}}$ and the $T_{c\text{-zero}}$, the temperature derivative of resistivity ($d\rho/dT$) was evaluated. Fig. 13a displays $d\rho/dT$ across the full temperature range (30–300 K), while Fig. 13b highlights the superconducting transition region (82–96 K). The $T_{c\text{-onset}}$ was defined as the temperature where $d\rho/dT$ deviated from linearity, indicating the initiation of the superconducting transition, while $T_{c\text{-zero}}$ was identified as the temperature at which the resistivity dropped to zero [19].

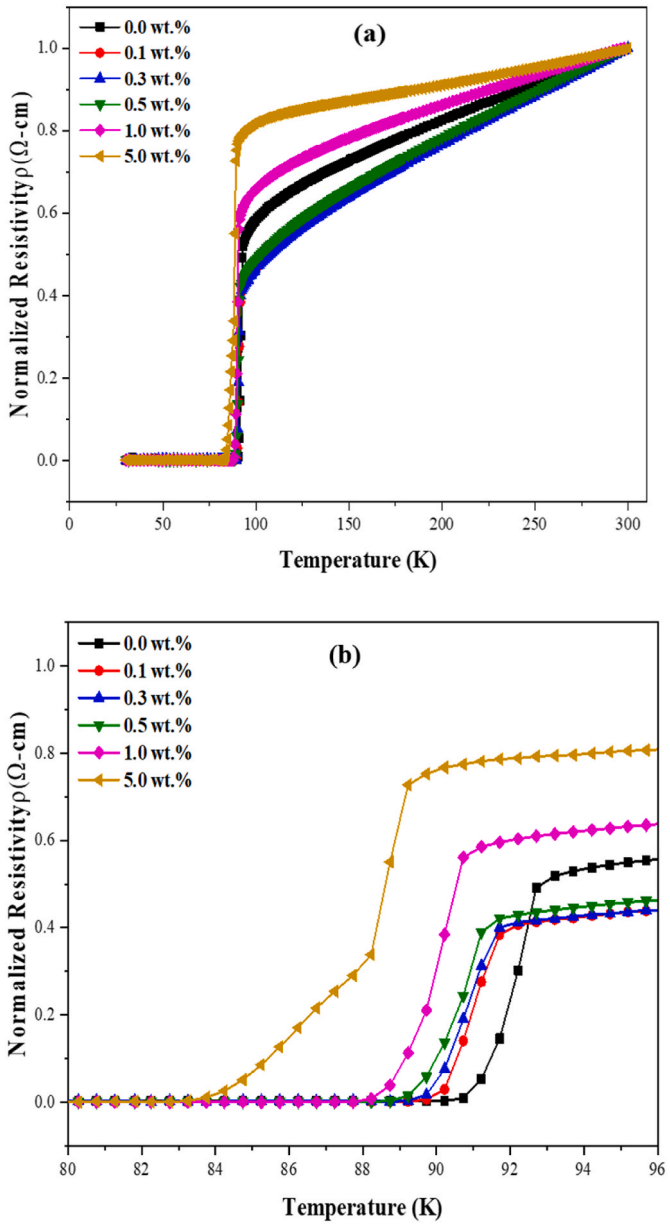

Fig. 12. **(a)** Temperature-dependent normalized resistivity of bulk Y-123 ceramics with varying Sm_2O_3 concentrations (0.0–5.0 wt%); **(b)** Magnified view of the superconducting transition region (80–96 K).

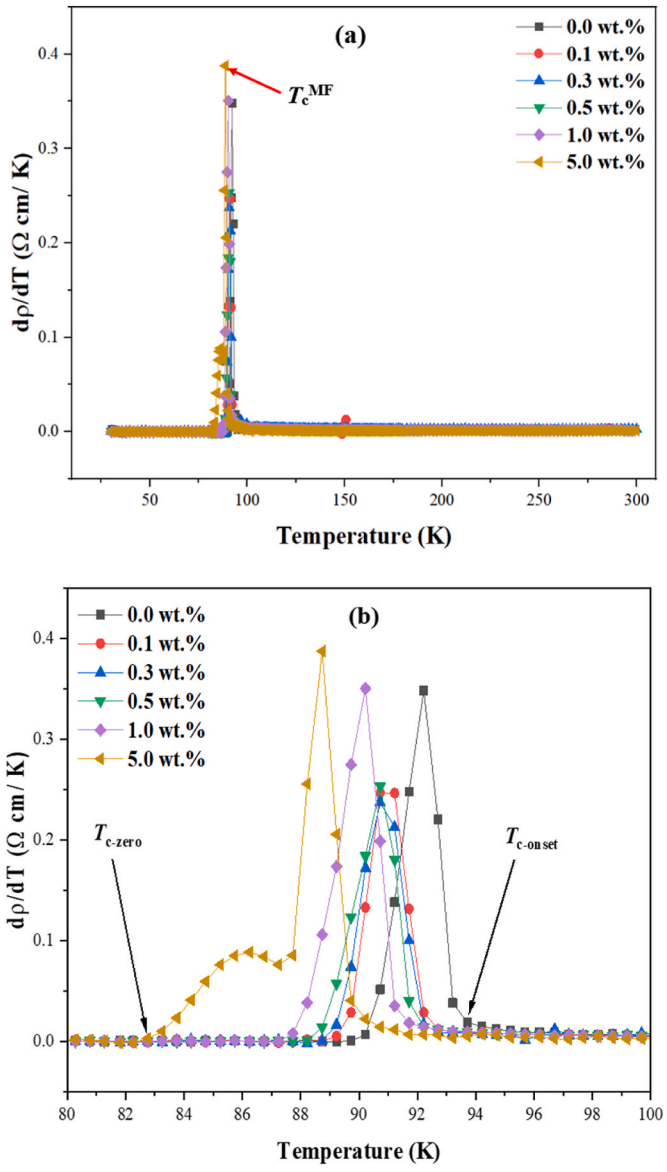

Fig. 13. **(a)** Temperature derivative of resistivity (dρ/dT) for Y-123 samples from 30 to 300 K; **(b)** Zoomed-in view of dρ/dT in the superconducting transition region (82–96 K).

Table 6 presents a summary of the critical superconducting parameters, including the $T_{c\text{-onset}}$, $T_{c\text{-zero}}$, ΔT_c, and hole concentration p. The results showed that the MTD technique improved the superconducting characteristics, particularly for the 0.1 wt% Sm_2O_3 sample, which exhibited the highest $T_{c\text{-onset}}$ and the narrowest ΔT_c. These improvements were attributed to the enhanced grain connectivity and optimized oxygen stoichiometry, thus reinforcing the advantages of controlled incorporation of Sm_2O_3 via MTD. A comparative evaluation with previous studies, such as Ramli et al. (2018) [16], supported these findings (see Table 6). The influence of the Sm_2O_3 concentration on the superconducting transition temperature is further depicted in Fig. 15. As the Sm_2O_3 content increased, the $T_{c\text{-onset}}$ gradually decreased, with the most significant broadening of ΔT_c and reduction in T_c being observed for the 5.0 wt% Sm_2O_3 sample. This behavior was consistent with the XRD and FESEM results, where excessive doping induced a secondary phase formation, increased porosity, and disrupted grain boundary networks. The elemental mapping results (Fig. 8) confirmed the uniform distribution of Y, Ba, Cu, O, and Sm in the 0.1 wt% sample, contributing to its enhanced superconducting behavior. In contrast, higher doping levels promoted compositional inhomogeneity and a degraded performance. The significant broadening of the superconducting transition and reduction in $T_{c\text{-zero}}$ at higher Sm_2O_3 concentrations are attributed to variations in the hole carrier concentration (P) within the CuO_2 planes, which influenced the charge transport and vortex dynamics [15,16]. The value of p was calculated using the following equation [2,29]:

$$P = 0.16 - \left[\frac{\left(1 - \frac{T_{c-offset}}{Tc^{max}_{-offset}}\right)}{82.6}\right]^{0.5} \quad (4)$$

where, T_c^{max} represents the maximum $T_{c\text{-onset}}$ observed across all the samples and (P) denotes the hole carrier's density in the CuO_2 planes.

As can be seen in Table 6, the introduction of Sm_2O_3 led to a gradual decrease in P, from 0.160 in the undoped sample to 0.137 in the 5.0 wt% Sm_2O_3 sample. Previous studies emphasized that maintaining an optimal p value (~0.160 holes per Cu atom) is critical for maximizing

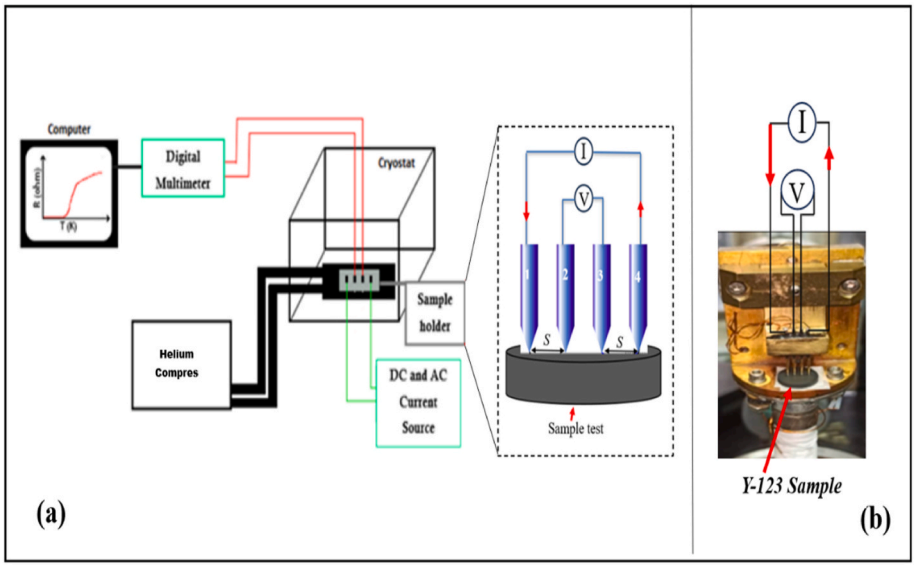

Fig. 14. **(a)** Schematic of the four-point probe (4 PP) resistivity measurement setup; **(b)** Photograph of the experimental sample holder.

Table 6
Critical onset temperature ($T_{c\text{-onset}}$), zero resistance temperature ($T_{c\text{-zero}}$), superconducting transition width (ΔT_c), and hole concentration (p) of Y-123 ceramics with Sm_2O_3 addition.

Sm_2O_3 Addition wt.%	$T_{c\text{-}onset}$ (K) ±	$T_{c\text{-}zero}$ (K) ±	ΔT_c (K) ±	T_c^{MF} (K) ±	$\Delta T_c^{MF\text{-}zero}$ (K) ±	Hole concentrations p	Ref.
0.0	93.71	90.22	3.49	92.21	1.99	0.160	This work
0.1	92.21	89.25	2.96	91.21	1.96	0.146	
0.3	92.21	88.73	3.48	90.72	1.99	0.146	
0.5	91.71	88.22	3.49	90.72	2.50	0.144	
1.0	91.21	87.23	3.98	90.21	2.98	0.142	
5.0	89.72	82.25	7.47	88.73	6.48	0.137	
0.0	92	88	4.0	/	/	/	Ramli et al. (2018)
0.2	91	80	4.0	/	/	/	
0.4	90	74	16	/	/	/	
0.6	90	72	18	/	/	/	
0.8	89	74	15	/	/	/	
1.0	88	66	22	/	/	/	

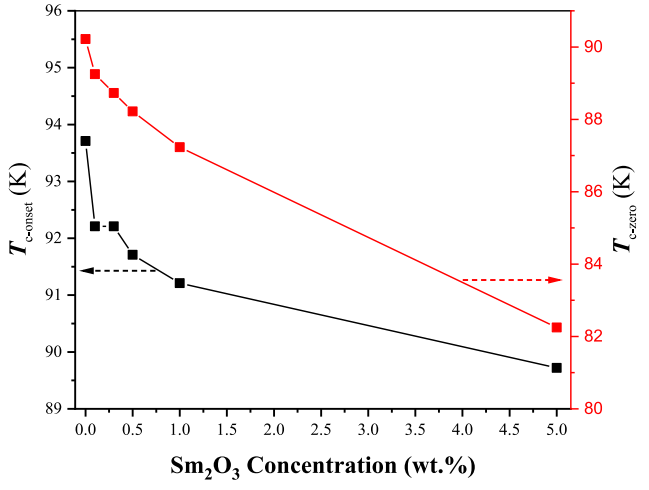

Fig. 15. Dependence of superconducting transition temperatures ($T_{c\text{-onset}}$ and $T_{c\text{-zero}}$) on Sm_2O_3 concentration in Y-123 ceramics.

the superconducting coherence length and T_c [2,50]. Despite the slight reduction in P, the 0.1 wt% Sm_2O_3 sample exhibited the highest J_c, highlighting those structural enhancements, such as improved flux pinning and enhanced grain connectivity, that can compensate for minor reductions in electronic carrier density. While an optimal P is important, microstructural refinement remains equally critical for achieving superior superconducting properties. These results confirmed that precise tuning of the Sm_2O_3 concentration via the MTD method effectively balanced the interplay between microstructure and electronic transport, establishing 0.1 wt% Sm_2O_3 as the optimal doping level for the maximization of superconducting performance [63,64].

4. Conclusions

In this study, bulk Y-123 ceramics were successfully synthesized with the additions of various concentrations of Sm_2O_3 (0.0–5.0 wt%) using a novel MTD method. Comprehensive structural and superconducting characterizations using XRD, FESEM, EDX, SQUID, and 4 PP techniques yielded the following major findings.

- XRD analysis with Rietveld refinement confirmed that all the samples retained the orthorhombic Y-123 phase, accompanied by minor secondary phases such as Y-211 and $BaCuO_2$. Notably, the 0.1 wt% of Sm_2O_3 sample exhibited the formation of a distinct Sm-123 secondary phase, contributing to enhanced phase stability, higher oxygen content (~6.87), increased crystallite size (~1865 Å), and reduced lattice strain, factors that collectively an improved phase formation and superconducting transition sharpness.

- FESEM analysis revealed that the 0.1 wt% Sm_2O_3-added sample achieved the largest average grain size (~8.14 μm) and the densest microstructure. At elevated doping levels (≥0.5 wt%), increased porosity, grain boundary disruptions, and deteriorated intergranular coupling.
- High-resolution cross-sectional FESEM imaging (50,000 ×) revealed zigzag grain morphologies and embedded nano-entities at 0.1 wt% of Sm_2O_3, acting as effective flux pinning centers. The EDX mapping confirmed a homogeneous elemental distribution and successful Sm incorporation without clustering.
- Electrical and magnetic measurements (4 PP and SQUID) showed that the 0.1 wt% Sm_2O_3-added sample achieved the highest critical current density ($J_c = 5.62$ kA/cm^2 at 77 K), with a $T_{c\text{-onset}}$ of 92.21 K, $T_{c\text{-zero}}$ of 89.25 K, and a narrow superconducting transition width ($\Delta T_c \approx 2.96$ K), reflecting strong flux pinning and minimal weak-link behavior. Conversely, higher doping levels adversely affected superconductivity due to structural and microstructural degradation.
- The MTD method proved to be a simple, scalable, and cost-effective synthesis route capable of producing high-performance Y-123 ceramics under ambient conditions. Its ability to uniformly incorporate Sm_2O_3 as a flux pinning agent and tailor microstructure highlighted its potential for the advancing next-generation high-temperature superconductors.

Declaration of competing interest

The authors declare that they have no known competing financial interests or personal relationships that could have appeared to influence the work reported in this paper.

Acknowledgments

Authors gratefully acknowledge financial support from the Ministry of Higher Education Malaysia (MOHE) for the Fundamental Research Grant Scheme FRGS/1/2019/STG02/UPM/02/3 (5540282) Universiti Putra Malaysia. The paper was partly supported by Japan Science and Technology (JST) for the advanced Project Based Learning (aPBL) at Shibaura Institute of Technology (SIT) under the Top Global University Project designed by the Ministry of Education, Culture, Sports, and Science & Technology, Japan. Syahrul Humaidi would like to thank LP USU under scheme PKUU-PT QS WUR RANK 101 300 LPDP No: 21709.1/UN5.4.17/TPM/2023 tanggal December 28, 2023.

References

[1] Hawsey AR, Christen k David. Progress in research, development, and pre-commercial deployment of second generation HTS wires in the USA. Phys 2006;C:488–95. https://doi.org/10.1016/j.physc.2006.04.062. 2006/10/01/.

[2] Yap SH, et al. Fluctuation induces conductivity and microstructural studies in Y-123: effect of CaO inclusion. J Alloys Compd 2024;1005:175955. https://doi.org/10.1016/j.jallcom.2024.175955. 2024/11/15/.

[3] Dadras SL, Chai Y, Daadmehr YS, V, Kim KH. Increase of critical current density with doping carbon nano-tubes in $YBa_2Cu_3O_{7-\delta}$. Phys. 2009;C:55–9. https://doi.org/10.1016/j.physc.2008.11.004. 2009/01/01/.

[4] Tsuchiya JAY, Ichino Y, Miura S, Yoshida Y. In-field transport properties at grain boundaries in $BaHfO_3$-doped $SmBa_2Cu_3Oy$ bicrystal films at low temperatures. IEEE Trans Appl Supercond 2019:1–5. https://doi.org/10.1109/TASC.2019.2903469.

[5] Mikheenko ASP, Dang VS, Tanner JL, Awang Kechik MM, Abell JS, Crisan A. Pinning centers induced in YBCO films by nano-dots in substrate decoration and quasi-superlattice approaches. IEEE Trans Appl Supercond 2009:3491–4. https://doi.org/10.1109/TASC.2009.2018307.

[6] Rejith PP, Vidya Sukumariamma, Vipinlal, Solomon Sam, Thomas Jijimon Kumpukattu. Flux-pinning properties of nanocrystalline HfO_2 added $YBa_2Cu_3O_7$ superconductor. Phys. Status Solidi B 2014:809–14. https://doi.org/10.1002/pssb.201349019.

[7] Ramli A, Shaari Abdul Halim, Baqiah Hussein, Kean Chen Soo, Mohd Mustafa Awang Kechik, Talib Zainal Abidin. Role of Nd_2O_3 nanoparticles addition on microstructural and superconducting properties of $YBa_2Cu_3O_{7-\delta}$ ceramics. J Rare Earths 2016:895–900. https://doi.org/10.1016/S1002-0721(16)60112-6. 2016/09/01/.

[8] Sahoo BR, Samal Krutika L, Behera D, Dhrubananda. "Effect of artificial pinning centers on YBCO high temperature superconductor through substitution of graphene nano-platelets,". Mater Chem Phys 2019:784–8. https://doi.org/10.1016/j.matchemphys.2018.11.048. 2019/02/01/.

[9] Volochová D, Antal V, Kováč J, Diko P. YBCO bulk superconductors with Sm addition. Mater Sci Forum 2017;891:483–8. https://dx.doi.org/10.4028/www.scientific.net/MSF.891.483.

[10] Volochová DD, Piovarči P, Antal S, Kováč V, Jirsa M. The effect of Sm addition on the microstructure and superconducting properties of YBCO bulk superconductors. Acta Phys. Pol. A 2017:1009–11. https://bibliotekanauki.pl/articles/1054772.pdf.

[11] Vojtkova PDL, Rajňák M. Influence of Sm_2O_3 and La_2O_3 additions on the microstructure and properties of YBCO bulk superconductors prepared by TSIG process. IEEE Trans Appl Supercond 2018:1–4. https://doi.org/10.1109/TASC.2018.2797981.

[12] A. G. M. Agarwal, Miryala. "Enhancing the superconducting properties of bulk (Sm, Eu,Gd)$Ba_2Cu_3O_{7-\delta}$: impact of BaO_2 and Ag_2O addition via infiltration growth process in air,". J Appl Phys 2025. https://doi.org/10.1063/5.0248525.

[13] Hajilou R, Sedghi Gamchi H. Irreversibility line and enhancement of magnetic flux pinning in Sm-doped Y123 superconductor with CuO nanoparticles. J Low Temp Phys 2020;198(1):70–89. https://doi.org/10.1007/s10909-019-02244-0. 2020/01/01.

[14] Güdücü G, et al. Assessment of superconducting and structural stability of advanced Y-123 and Y-358 ceramics with Tb/Y substitution in main matrices. J Alloys Compd 2024;997:174838. https://doi.org/10.1016/j.jallcom.2024.174838. 2024/08/30/.

[15] Vojtkova LD, Kovac P, Vojtko J, M. Influence of Sm_2O_3 microalloying and Yb contamination on Y211 particles coarsening and superconducting properties of IG YBCO bulk superconductors. Supercond Sci Technol 2018:065003. https://doi.org/10.1088/1361-6668/aabb4e. 2018/04/26.

[16] Aima SAHR, Chen SK, Awang Kechik MM. The effect of Sm_2O_3 nanoparticle inclusion on superconducting properties of YBCO ceramics. Sci. J. Spec. Issue, no. ASM Sci. J.Special Issue 2018;2018(1):45–9. AiMS2018, 8-16, https://www.akademisains.gov.my/asmsj/?mdocs-file=3523.

[17] Sah NAMIA, et al. Comparative studies of pure $YBa_2Cu_3O_{7-\delta}$ prepared by modified thermal decomposition method against thermal treatment method. Appl. Phys. A 2024;130(5):340. https://doi.org/10.1007/s00339-024-07412-y. 2024/04/25.

[18] Ochsenkühn-Petropoulou M, et al. Comparison of the oxalate co-precipitation and the solid state reaction methods for the production of high temperature superconducting powders and coatings. J Mater Process Technol 2002;127(1):122–8. https://doi.org/10.1016/S0924-0136(02)00279-0. 2002/09/20/.

[19] Arebat RAM, Kechik MMA. $YBa_2Cu_3O_{7-d}$ bulk superconductors: exploring the impact of two synthesis techniques on the microstructure and critical temperature. Solid State Sci. Technol. 2024;(28–41%V 32) 2024-05-12, https://myjms.mohe.gov.my/index.php/masshp/article/view/25985.

[20] Asikuzun E. Production procedure and characterization of Zn-doped Y-123 superconducting samples prepared by sol-gel method. J Supercond Nov Magnetism 2018;31(11):3509–14. https://doi.org/10.1007/s10948-018-4735-3. 2018/11/01.

[21] Dihom MM, et al. Microstructure and superconducting properties of Ca substituted $Y(Ba_{1-x}Ca_x)_2Cu_3O_{7-\delta}$ ceramics prepared by thermal treatment method. Results Phys 2017;7:407–12. https://doi.org/10.1016/j.rinp.2016.11.067. 2017/01/01/.

[22] Dihom MM, et al. Effects of calcination temperature on microstructure and superconducting properties of Y123 ceramic prepared using thermal treatment method. Solid State Phenom 2017;268:325–9. https://dx.doi.org/10.4028/www.scientific.net/SSP.268.325.

[23] Mohd Hapipi NS, Halim Abdul, Kechik MMAT, Ban Kar, Abd-Shukor RMS, Raihan Nurul, Chen SK. Effect of heat treatment condition on the phase formation of $YBa_2Cu_3O_{7-\delta}$ superconductor. Solid State Phenom 2017:305–10. https://dx.doi.org/10.4028/www.scientific.net/SSP.268.305.

[24] Arebat RAM, et al. Impact of calcination temperature on the microstructure and superconductivity of $YBa_2Cu_3O_{7-\delta}$ ceramic prepared via modified thermal decomposition method. J. Aust. Ceram. Soc. 2025. https://doi.org/10.1007/s41779-025-01172-5. 2025/03/17.

[25] Al-Gaashani R, Aïssa B, Anower Hossain M, Radiman S. Catalyst-free synthesis of ZnO-CuO-$ZnFe_2O_4$ nanocomposites by a rapid one-step thermal decomposition approach. Mater Sci Semicond Process 2019;90:41–9. https://doi.org/10.1016/j.mssp.2018.10.004. 2019/02/01/.

[26] Al-Gaashani R, Radiman S, Tabet N, Razak Daud A. Synthesis and optical properties of CuO nanostructures obtained via a novel thermal decomposition method. J Alloys Compd 2011;509(35):8761–9. https://doi.org/10.1016/j.jallcom.2011.06.056. 2011/09/01/.

[27] Yap SH, et al. Comparing study of electrical transport properties of bulk Y-123 synthesized by modified wet and dry synthesis methods. Solid State Sci. Technol. 2025:107921. https://doi.org/10.1016/j.solidstatesciences.2025.107921. 2025/04/09/.

[28] Arebat RAM, et al. Influence of oxygen flow vs. ambient annealing on microstructure and superconducting properties of $YBa_2Cu_3O_{7-\delta}$ bulk ceramics. J Mater Sci Mater Electron 2025;36(12):760. https://doi.org/10.1007/s10854-025-14827-7. 2025/04/28.

[29] Arebat RAM, et al. Enhancing superconducting properties of $YBa_2Cu_3O_{7-\delta}$ through Nd_2O_3 addition prepared using modified thermal decomposition method. Appl. Phys. A 2024;130(12):897. https://doi.org/10.1007/s00339-024-08035-z. 2024/11/18.

[30] Delorme F, Harnois C, Monot-laffez I. Additions of 0.5 wt% of rare earth oxides to TSMTG $YBa_2Cu_3O_{7-\delta}/Y_2BaCuO_5$ composites. Phys C Supercond 2003;399(3):129–37. https://doi.org/10.1016/S0921-4534(03)01301-7. 2003/12/01/.

[31] Hamoudi AR, May A, Henniche A, Ouyang J-H, Guillet A. A comparative study of (Ce) and (Gd) doping influence on the superconducting properties of YBCO ceramics. Ceram Int 2021;47(18):25314–23. https://doi.org/10.1016/j.ceramint.2021.05.253. 2021/09/15/.

[32] Almessiere MAS, Hannachi Y, Algarni E, Ben Azzouz R, F. "Impact of Dy_2O_3 nanoparticles additions on the properties of porous YBCO ceramics,". J Mater Sci Mater Electron 2019:17572–82. https://doi.org/10.1007/s10854-019-02106-1. 2019/10/01.

[33] Adin MŞ. Investigation of the effects of machining parameters on kerf widths during laser beam machining of medium carbon steels. J Mater Eng Perform 2025;34(6):5304–15. https://doi.org/10.1007/s11665-025-10889-0. 2025/03/01.

[34] H. Adin, S. Akgül, and M. Ş. Adin, "Effect of silver nanopowder addition on mechanical properties of silver-copper alloy used in the jewellery industry," Proc Inst Mech Eng, Part E, vol. 0, no. 0, p. 09544089251316320, doi: 10.1177/09544089251316320.

[35] Naito N, Kafalas J, Jachim L, Downey M. Effect of humidity on chemical stability and superconductivity of YBa2Cu3O7−x. J Appl Phys 1990;67(7):3521–3. https://doi.org/10.1063/1.345345.

[36] Chen DXG, B R. Kim model for magnetization of type-II superconductors. J Appl Phys 1989:2489–500. https://doi.org/10.1063/1.344261.

[37] A. G. M. Agarwal, Muralidhar. Advancing processing of the ternary (Sm,Eu,Gd) $Ba_2Cu_3O_{7-y}$ superconductor via top-seeded infiltration growth. Ceram Int 2024:31559–66. https://doi.org/10.1016/j.ceramint.2024.05.463. 2024/09/01/.

[38] Yao XN, Tagami M, Shiohara M, Y. Growth rate and superconductivity of Y(Sm)BCO single crystals. Phys. 1996;C:227–32. https://doi.org/10.1016/S0921-4534(96)00571-0. 1996/12/01/.

[39] Kamarulzaman MMH, Adam SA, Faisal MI, M A M. Structure and superconductivity in $YBa_2Cu_3O_{7-\delta}$ with additives of nano-Sm_2O_3. AIP Conf Proc 2010:492–5. https://doi.org/10.1063/1.3469717.

[40] Jian H, et al. Oxygen order control by post-annealing for optimizing critical temperature of YBaCuO coated conductors with silver protective layer. Phys C (Amsterdam, Neth) 2017;538:40–5. https://doi.org/10.1016/j.physc.2017.05.007. 2017/07/15/.

[41] Benzi P, Bottizzo E, Rizzi N. Oxygen determination from cell dimensions in YBCO superconductors. J Cryst Growth 2004;269(2):625–9. https://doi.org/10.1016/j.jcrysgro.2004.05.082. 2004/09/01/.

[42] Patterson AL. The scherrer formula for X-ray particle size determination. Phys Rev B 1939:978–82. https://doi.org/10.1103/PhysRev.56.978.

[43] Saghafi MS, Soltani Gholamabbas, Zahra. The influence of Sm_2O_3 nanoparticles adding on some superconducting properties of $Bi_{1.6}Pb_{0.4}Sr_2Ca_2Cu_3O_{10+\delta}$ ceramics. Phys 2024;C:1354566. https://doi.org/10.1016/j.physc.2024.1354566. 2024/09/15/.

[44] N. A. Dzul-Kifli et al., "Superconducting Properties of $YBa_2Cu_3O_{7-\delta}$ with a Multiferroic Addition Synthesized by a Capping Agent-Aided Thermal Treatment Method," Nanomater., doi: 10.3390/nano12223958.

[45] Akhtar M, et al. Phase transformations and numerical modelling in simulated HAZ of nanostructured P91B steel for high temperature applications. Appl Nanosci 2018;8(7):1669–85. https://doi.org/10.1007/s13204-018-0854-1. 2018/10/01.

[46] Crisan AAK, Mikheenko MM, Dang P, Sarkar VS, Abell A, Paturi JS, Huhtinen P, H. Critical current density and pinning potential in $YBa_2Cu_3O_{7-\delta}$ thick films ablated from a $BaZrO_3$-doped nanocrystalline target. Supercond Sci Technol 2009:045014. https://doi.org/10.1088/0953-2048/22/4/045014. 2009/03/17.

[47] Murakami MY, Fujimoto K, Nakamura H, Taguchi N, Koshizuka T, Tanaka N, S. Flux pinning by non-superconducting inclusions in melt-processed YBaCuO superconductorrs. Cryogenics; 1992/01/01/1992. p. 930–5. https://doi.org/10.1016/0011-2275(92)90002-R.

[48] W. B. Nowak, Michał Hanc-Kuczkowska, Aneta and P. P. Sobota, Adam Idczak, Rafał, "Effect of the Presence of Structural Defects on the Superconducting Properties of $(NbTa)_{0.67}(MoHfW)_{0.33}$ and $Nb_{.47}$ wt%Ti," Met. , doi: 10.3390/met13101779.

[49] Mannhart JB, Goetz H, Hilgenkamp B, Schmehl H, Schneider A, Schulz CW, R R. Grain boundaries in high-T_c superconductors: insights and improvements. Philos Mag 2000;B:827–34. https://doi.org/10.1080/01418630008221948. 2000/05/01.

[50] K MMA, Yap Siew Hong, Fitri Khoerunnisa b, et al. Microstructural and excess conductivity properties of Y-123: effect of organic polymer chitosan inclusion. J Mater Sci Mater Electron 2024:1452. https://doi.org/10.1007/s10854-024-13161-8. 2024/07/22.

[51] Chong TVL, King Liow Shin, Han Abd-Shukor Chiew, Roslan. Effects of carbon nanotubes addition on the superconducting properties and critical current density of $NdBa_2Cu_3O_{7-\delta}$. Appl. Phys. A:Solids Surf. 2022:740. https://doi.org/10.1007/s00339-022-05877-3. 2022/08/04.

[52] Wang PFZ, Jin GF, Yan LH, Shen WW, Wang Y, Li Y, Lu CS, Y F. Effects of Sm-doping on structures and properties of YBCO coated conductors fabricated by TFA-MOD process. J. Supercond. Novel Magn. 2012:261–6. https://doi.org/10.1007/s10948-011-1294-2. 2012/02/01.

[53] A. Khajuria, S. S., and A. and Misra, "Comparative study of fillers for welding E410 structural steel," Adv. Technol. Mater. Process. J., pp. 1-21, doi: 10.1080/2374068X.2024.2379691.

[54] Khajuria A, Misra A, Shiva S. The influence of CMT-MAG and MAG welding-processes on microstructure and mechanical behaviour of C-Mn E410 structural-steels. Int J Mater Struct Integr 2024;15(2):322–42. https://doi.org/10.1108/IJSI-12-2023-0141.

[55] Shih-Yun CP-C, Hseih, In-Gann, Maw-Kuen Chen, Wu. Effect of nano-scale additions on the superconductivity and pinning mechanism in the Sm-Ba-Cu-O materials. Chin J Phys 2005:666–74. https://doi.org/10.6841/NTUT.2007.00127 (in 英文).

[56] Algarni R, Almessiere MA, Slimani Y, Hannachi E, Ben Azzouz F. Enhanced critical current density and flux pinning traits with Dy_2O_3 nanoparticles added to $YBa_2Cu_3O_{7-d}$ superconductor. J Alloys Compd 2021;852:157019. https://doi.org/10.1016/j.jallcom.2020.157019. 2021/01/25/.

[57] Mikheenko JSAP, Sarkar A, Dang VS, Awang Kechik MM, Tanner JL, Paturi P, Huhtinen H, Hari Babu N, Cardwell DA, Crisan A. Self-assembled artificial pinning centres in thick YBCO superconducting films. J. Phys.:Conf. Ser. 2010:022022. https://doi.org/10.1088/1742-6596/234/2/022022. 2010/06/01.

[58] Jirsa MPu, Dlouhý L, Koblischka D, M R. Fishtail shape in the magnetic hysteresis loop for superconductors:Interplay between different pinning mechanisms. Phys Rev B 1997:3276–84. https://doi.org/10.1103/PhysRevB.55.3276.

[59] Krabbes GF, Canders G, May WR, Palka H, R. High temperature superconductor bulk materials: fundamentals, processing, properties control, application aspects. Wiley; 2006.

[60] Muralidhar MJ, Sakai Milos, Murakami Naomichi, Masato. Improvement in field trapping capability of (Nd,Eu,Gd) $Ba_2Cu_3O_y$ with Ag_2O addition. Jpn J Appl Phys 2001:6329. https://doi.org/10.1143/JJAP.40.6329. 2001/11/01.

[61] Khajuria A, Shiva S, Misra A. The carbon content effect on hot-rolled C–Mn micro-alloyed E410 structural steel. Vacuum 2023;212:112042. https://doi.org/10.1016/j.vacuum.2023.112042. 2023/06/01/.

[62] Khajuria A, Misra A, Shiva S. On the heat-affected zone role for mechanical properties of structural-steel MIG and CMT–MIG weldments. Trans. Indian Inst. Met. 2024;77(11):3905–13. https://doi.org/10.1007/s12666-024-03460-3. 2024/11/01.

[63] Naqib SHI, R S. Possible quantum critical behavior revealed by the critical current density of hole doped high-T_c cuprates in comparison to heavy fermion superconductors. Sci Rep 2019:14856. https://doi.org/10.1038/s41598-019-51467-4. 2019/10/16.

[64] Ahmad NN, S H. Estimation of Cooper pair density and its relation to the critical current density in Y(Ca)BCO high-T_c cuprate superconductors. Results Phys 2020:103054. https://doi.org/10.1016/j.rinp.2020.103054. 2020/06/01/.